Nuclear Materials Authority
P.O.Box 530 Maadi, Cairo, Egypt

ISSN 2314-5609
Nuclear Sciences Scientific Journal
9, 227- 253
2020
http://www.ssnma.com

APPLICATION OF REMOTELY SENSING DATA IN THE GEOLOGIC AND RADIOACTIVE MAPPING OF WADI FATIRAH PRECAMBRIAN ROCKS, NORTH EASTERN DESERT, EGYPT

MOHAMED S. HAMMED; NAHLA A. SHALLALY; ISMAIL M. ABDEL GHANI[1]; YASSER S. BADR[1]; SABREEN A. SAYED[1]

Dept. Geol., Fac. Sciences, Cairo Univ.; [1]Nuclear Materials Authority, Cairo, Egypt

ABSTRACT

The present study aims to integrate spectral analysis results of multispectral Landsat-8 and ASTER data besides airborne gamma-ray spectrometric data in geologic and radiometric mapping as well as alteration types of Wadi Fatirah area, North Eastern Desert, Egypt. The applied image processing techniques comprising Color Band Composites, Principal Component Analysis, Crosta technique and Band Ratio were efficient in lithological units discrimination and alteration types identification. The airborne gamma-ray spectrometric maps discriminate the younger granites in the study area but it could not differentiate between their phases. The remote sensing products are verified by detailed field, petrographic and radiometric analysis. The results are elaborated as a precise geological map of 1:50,000 scale with metavolcanics (oldest), older granitoids, Dokhan volcanics, younger gabbros, younger granites and post granitic dikes and pegmatites (youngest) rock units, and tracing the hydrothermal alterations in form of propylitic, phyllic and gossan as well as illite, kaolinite, limonite, hematite, ferromagnesian and hydroxyl distribution maps. Additionally, the radioactive anomalies are mainly related to the younger granites and pegmatite bodies that mainly associated with ferrugination (iron oxides and hydroxides alteration). The most promising radioactivity are delineated as pegmatite bodies at Wadi Abu Zawal and Wadi Abu Shihat.

INTRODUCTION

Geological mapping and mineral exploration are some of the main responsibilities of remote sensing applications. Nowadays, remote sensing data is usually utilized for lithological mapping, structure analysis and mineral exploration around the world, particularly in the arid and semi-arid regions (e.g. Abdeen and Greiling, 2005; Rowan, et al., 2005; Acharya and Mallik, 2012; Arnous and Sultan, 2014; El-Said, 2014; Sweha, 2014; Badr, 2017 and Abdel Ghani, 2020). In the last decades, the Nuclear Materials Authority (NMA), conducted comprehensive programs for exploration for uranium mineralization in Egypt. These programs led to the discovery of some U-mineralization related to the so-called younger granites (Gabal [G.] El-Erediya, G. El-Missikat, G. Gattar, G. Um Ara-Um Shilman, El Sella and Abu Rushied younger granites plutons), in the Eastern Desert of Egypt (ED). Gamma-ray survey method has been applied extensively in support of geological mapping and mineral exploration since 1970s.

It has been found to be suitable for mapping granites and their internal zonation (Gossens, 1992; Welman, 1998 and Schetselaar, 2001). In addition, the use of gamma-ray spectrometry enables alteration mapping in a wide range of geologic settings (Daviz and Guilbert, 1973; Kuhns, 1986 and Schroeter, 1995). The Egyptian basement rocks constitute the northwestern tip of the Arabian-Nubian Shield that represents the northern part of the U-shaped Pan-African orogenic belt of Africa. The age of the Arabian-Nubian Shield ranges between 600 and 1000 Ma (Fullagar and Greenberg, 1978; Dixon, 1979 and Hashad, 1980) or between 450 and 1200 Ma (Gass, 1981).

The present work was planned for Wadi (W.) Fatirah area because of the presence of several younger granites plutons and their similarity to those ones with radioactive potentiality such as G. El Missikat and G. Gattar beyond the southern and northern limits of the study area respectively. The study area is located in the North Eastern Desert (NED), bounded by lat. 26°36`50`` and 26°50`23``N and long. 33°16` 37``and 33°29`31``E. W. Fatirah area is accessible from the Qena-Safaga asphaltic road at km 85 east Qena city (Fig. 1a). The study area is characterized by a rugged topography due to presence of high mountains like Gabal (G) Abu Kharif (1388m a.s.l). The area are traversed by several wadis such as W. Abu Shihat, W. Abu Zawal (ENE-WSW), which drains west-wards to W. Fatirah (E-W), W. Fatirah El-Beidah, W. Fatirah El-Zarqah (NE-SW), which also drain southwest-wards at W. Fatirah (E-W) just beyond the western limit of the study area (Fig. 1b). The current study aims for achieving the following: a) Discriminating the different Precambrian rock units and construct a detailed geological map for the study area, b) Tracing the various alteration zones and c) Defining the prospect of high radioactive potential and their lithology.

MATERIALS AND METHODS

In the present work, three types of remotely sensed datasets were used: a) single Landsat-8 L1T (terrain corrected) scene (path174 / row 42) of UTM projection, zone 36 N and WGS-84 datum, acquired in October. 6, 2018, cloud-free, with scene ID LC81740422018279LGN00, is obtained from the USGS Earth Explorer site *(http://earthexplorer.usgs.gov/);* b) ASTER L1B (Radiance at Sensor) scene ASTL1B07100708361108 09120036 of the study area was downloaded from NASA Land Processes Distributed Active Archive Center (LPDAAC). Both of them were atmospherically corrected using the Fast Line of Sight Atmospheric Analysis of Spectral Hypercube (FLAASH). ASTER VNIR and SWIR bands were spatially resized to 30m x 30m pixels using the nearest neighbor algorithm to preserve SWIR bands spectral characteristics (Galvão et al., 2005). Image processing techniques including Color Band Composites (CBC), data transformation techniques such as Band Rationing (BR), Principal Component Analysis (PCA) and feature oriented principal component selection (Crosta technique) were performed in this study. These techniques are widely applied for lithological mapping and mineral exploration (e.g.Abrams et al., 1983; Sabins, 1987; Crosta and Moore 1989; Loughlin, 1991; El-Rakaiby, 1993; Abdelsalam et al., 2000; Abdeen et al., 2001; Rowan et al., 2003; Velosky et al., 2003; Xu et al., 2004; Badr, 2017; Dawoud et al., 2017 and Abdel Ghani, 2020). All processing was carried out using software packages including ENVI 5.3, Arc GIS 10.5 and Global Mapper 20; c) The airborne gamma-ray spectrometric data of the study area was acquired in 1984. The survey was carried out along parallel flight lines oriented in a NE-SW direction at one km spacing, while the tie lines were flown in NW-SE direction at 10 km intervals at a nominal flight altitude of 120 m terrain clearance *(*Aero-Service, 1984*)*. All the aero-spectrometric data (eU, eTh, K and total count, TC, values) are multiplied by 10. The data were processed and resulted in three radioelements maps of eU, eTh and K besides a radioelements composite ternary map that

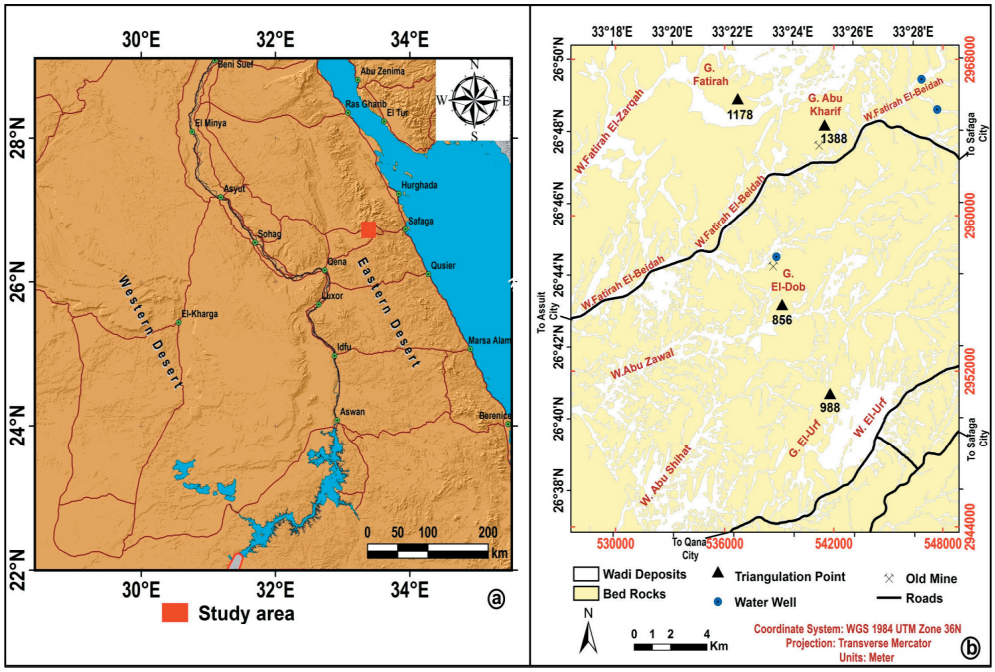

Fig. 1: Location map (a) and physiographic map (b) of W. Fatirah area, NED, Egypt

used to clarify both lithological mapping and radioelements potentiality. These spectrometric data also treated qualitatively and quantitatively by gamma-ray spectrometric techniques to stand on the radioactive anomalies in the study area. The airborne gamma-ray spectrometric data were processed using Geosoft Oasis Montaj software (version 8.3.3). The steps that are carried out through this work are shown on (Fig. 2).

The spectral profiles of the seven exposed rock units in the study area show the reflectance behavior of such seven rock units over the different bands of the Landsat-8 and ASTER data. Thus, the different rock units, which are covering the study area, were carefully discriminated using different band ratios. In this study, the spectral signature profiles that were extracted from the VNIR and SWIR OLI and ASTER data (Fig. 3a&b) were considered as the basic criteria for choosing the band ratios transformation.

Fieldwork is carried out to check the occurrence and spatial distribution of the lithological units. During the field work, the interpreted images were checked and verified in order to stand on the rock types and their contacts as well as their alteration types and their distribution. Representative samples from the different rock units and their alteration products were collected for petrographic and radiometric studies. Finally, an accurate assessment of the results of the field check and petrographic studies was done.

The microscopic studies and photomicrographs were carried out using a CMOS color camera (SC180) polarizing microscope equipped with a fully automatic photomicrographic attachment (Olympus PX53). All the above-mentioned studies and the radiometric analyses were carried out in the laboratories of the Egyptian Nuclear Materials Authority.

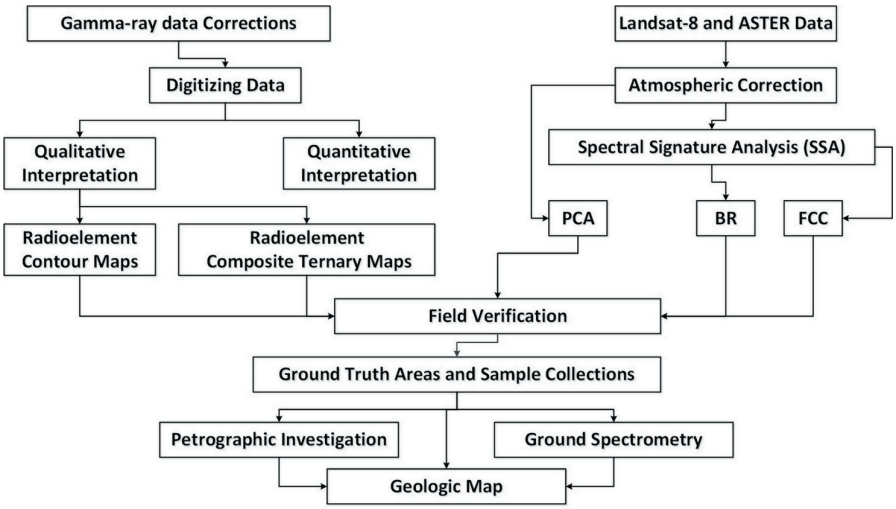

Fig. 2: Flowchart of the main processing steps that performed in the present study

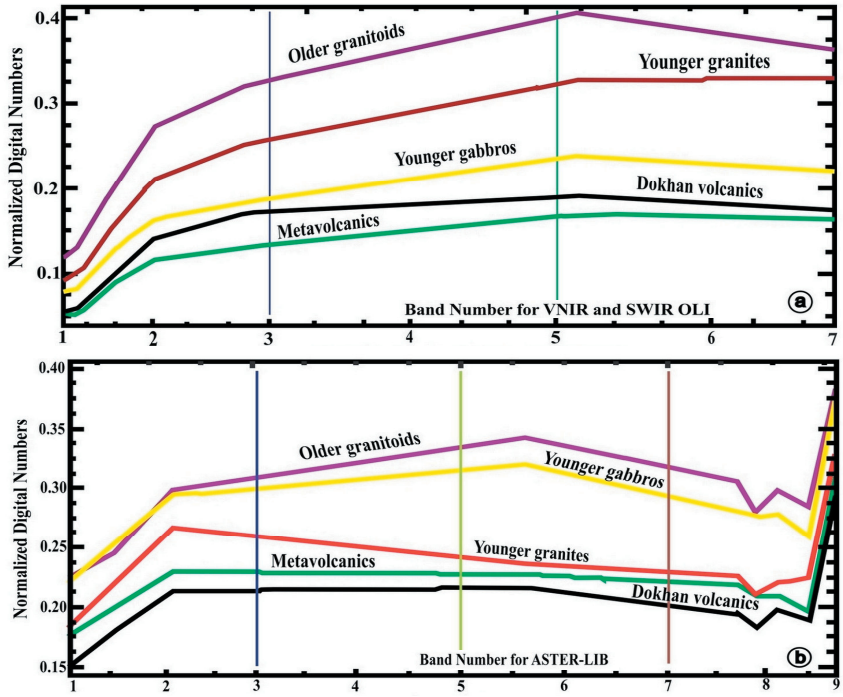

Fig. 3: Spectral signature profiles of the mapped rock units by Landsat-8 (a) and ASTER (b) data

RESULTS AND DISCUSSIONS

Image Processing Landsat-8 and ASTER Data

Color band composite (CBC)

A false-color composite image of Landsat-8 Bands (7, 5, 3 in RGB) was carried out (Fig. 4). The image represents different wavelengths (7 of SWIR, 5 of NIR, and 3 of visible green) hence gives the highest variance (Jensen, 1986). This image has the ability to discriminate against different rock units, especially traces the Dokhan volcanics, the metavolcanics and younger gabbros. In addition, the false-color composite image of ASTER Bands (7, 4, 2 in RGB) of (Rowan et al., 2005) is applied to enhance the structural features and exactly traced the older granitoids (Fig. 5).

Band rationing (BR)

Three landsat-8 band ratios (b4/b2, b5/b6 and b6/b7) were created to delineate ferrugination, ferromagnesian and OH-bearing minerals respectively, revealed three grey scale images. The brightened areas represent the high concentration of target minerals. The expected threshold anomalous of these band ratios are calculated at confidence level 95%. A band ratio b4/b2 enhanced iron oxides that have absorption in (band 2) and shows significant reflectance in (band 4), exactly traced the Dokhan volcanics as well as the younger granites and isolates them from the other rock units in the study area (Fig. 6). Band ratio b5/b6 enhances ferromagnesian minerals (Fig. 7) exactly traces the boundaries of the Dokhan volcanics as they are of intermediate composition. Band ratio b6/b7 enhances carbonates and OH-bearing minerals (Fig. 8) roughly traces the Dokhan volcanics, the metavolcanics and parts of the older granitoids in the southeastern part of the study area as well as syenogranites north G. El-Dob.

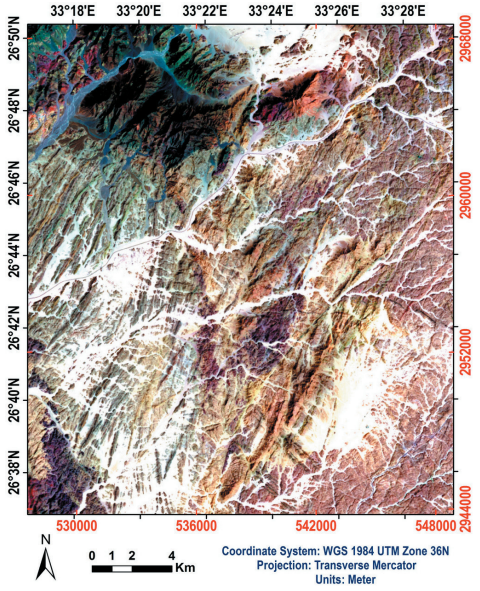

Fig. 4: False color composite Landsat 8 image bands 7, 5, 3 in RGB of W. Fatirah area, NED, Egypt

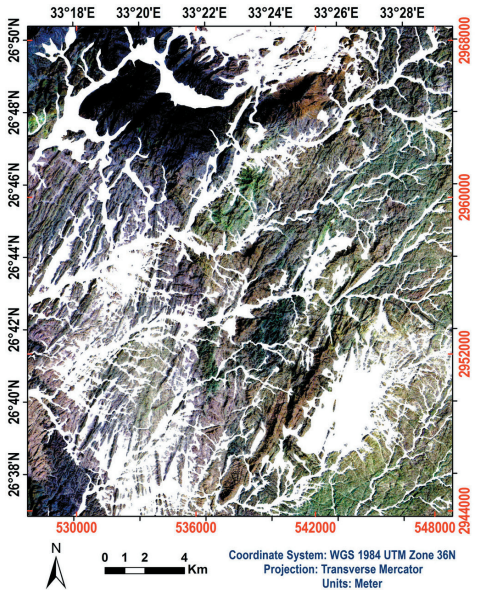

Fig. 5: False color composite ASTER image bands 7, 4, 2 in RGB of W. Fatirah area, NED, Egypt

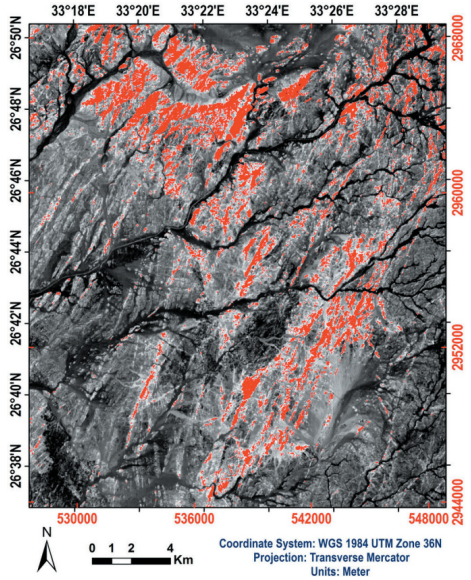

Fig. 6: Ferrugination (Landsat-8 ratio b4/b2) of W. Fatirah area, NED, Egypt (red color is theexpected threshold anomalies at 95% confidence)

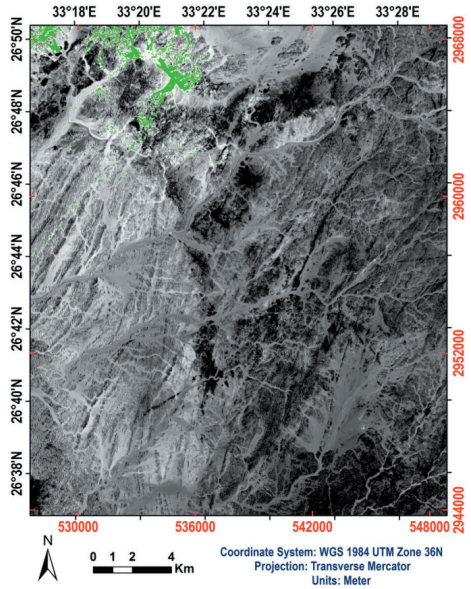

Fig. 7: Ferromagnesian minerals (Landsat-8 ratio b5/b6) of W. Fatirah area, NED, Egypt (green color is the expected threshold anomalies at 95% confidence)

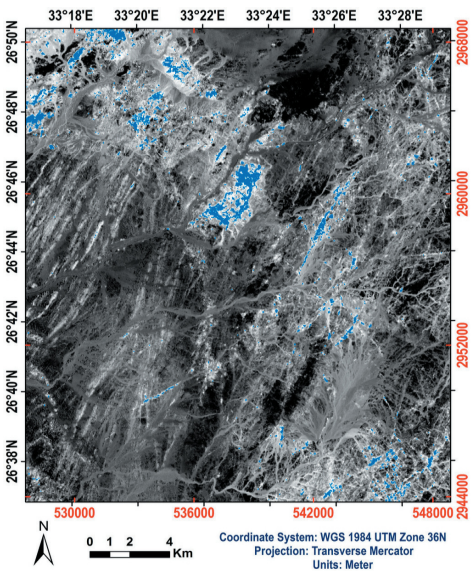

Fig. 8: Carbonates and OH-bearing minerals (micas and clays) minerals (Landsat-8 ratio b6/b7) of W. Fatirah area. NED, Egypt (blue color is theexpected threshold anomalies at 95% confidence)

Landsat-8 Color composite image for the three image ratios [(b4/b2), (b5/b6) and (b6/b7)] were assigned as RGB respectively, are created for the delineation of hydrothermal alteration zones (Fig. 9) and their color combinations. This composite image well distinguishes all the different rock units as follows: 1) The metavolcanics are incorporate into metabasalts (mixture of blue, magenta and brown colors) that are exposed at the northern periphery of W. Fatirah El-Zarqah and their pyroclastic that composed of tuffs and agglomerates (bluish green color) exposed at the southwestern corner of the study area; 2) the older granitoids appear as blue-violet with dark green colors at the eastern side of the study area; 3) the Dokhan volcanics appears as a mixture of blue and aquamarine colors; 4) The younger gabbros appears as deep blue color at the center of the area as well as the southwestern corner and finally; 5) the younger granites types; a) monzogranites

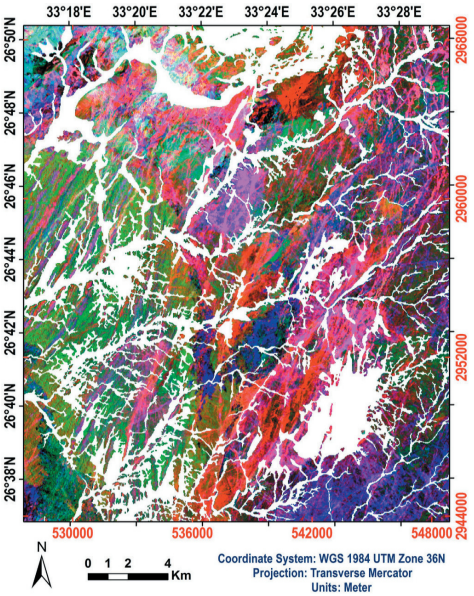

Fig. 9: Color composite of Landsat-8 ratio (b4/b2), (b5/b6), (b6/b7) in RGB of W. Fatirah area, NED, Egypt

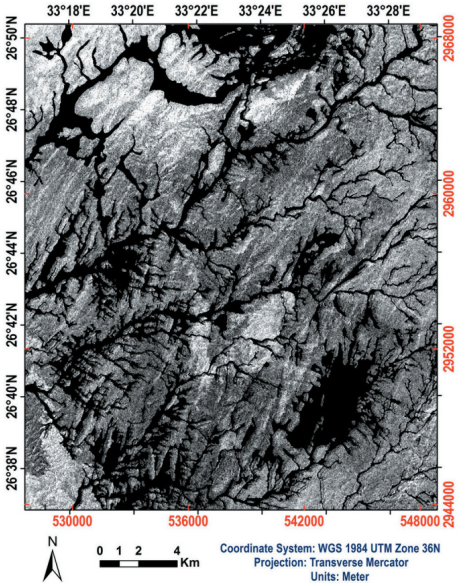

Fig.10: ASTER band ratio (b7+b9)/b8 image showing propylitic alteration in brightened areas of W. Fatirah area, NED, Egypt

(yellowish-green), b) syenogranites (magenta and orange dotted with brown colors) and c) alkali-feldspar granites (red color).

Propylitic alteration has an absorption centered at 2.35 µm, which coincides with ASTER band 8 caused by (Mg-OH). ASTER band ratio (b7+b9)/ b8 was created for (Mg-OH) enhancement (Fig. 10). This type of alterationis encountered accompanied with the basic rocks including metavolcanics, Dokhan volcanics and younger gabbros. Phyllic alteration is characterized by illite/muscovite (sericite) which yields an intense (Al-OH) absorption feature centered at 2.20 µm, ASTER band ratio (b5+b7)/ b6 was used for (Al-OH) enhancement (Fig. 11). This alteration type is characterizes the older granitoids, Dokhan volcanics and syenogranites. Gossan form by the oxidation of the sulfide minerals thus may be used as clues to the existence of subsurface ore deposits. Gossan is enhanced by ASTER band ratio (b4/b2) appears as brightened areas in (Fig. 12). This type of alteration occurred

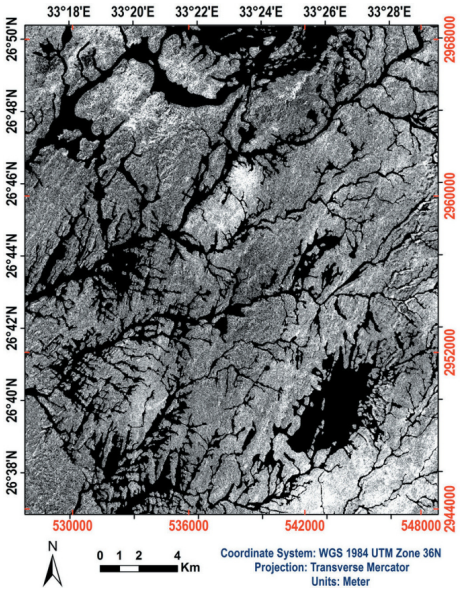

Fig. 11: ASTER band ratio (b5+b7)/b6 image showing phyllic alteration in brightened areas of W. Fatirah area, NED, Egypt

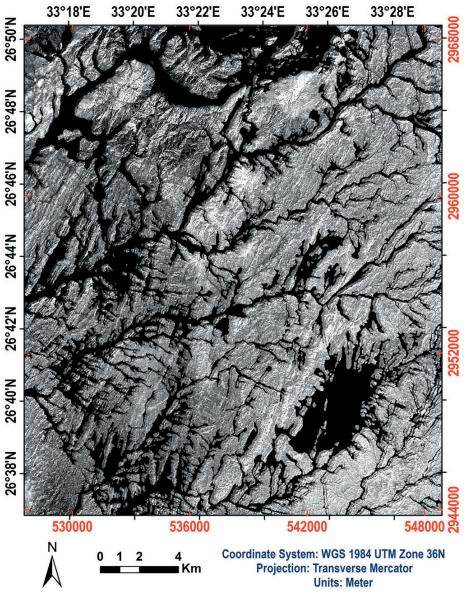

Fig. 12: ASTER band ratio (b4/b2) image showing gossan in brightened areas of W. Fatirah area, NED, Egypt

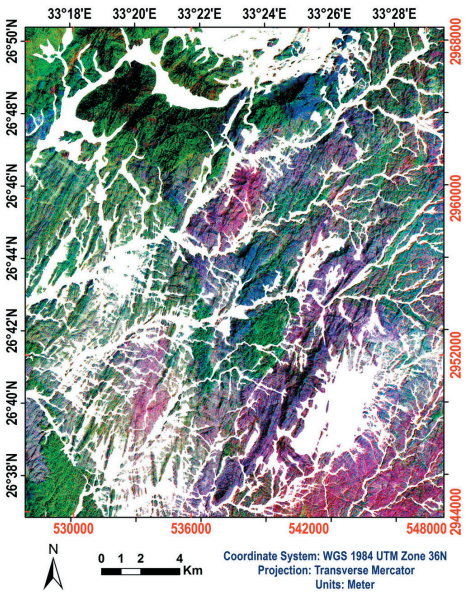

Fig.13: False color composite image of phyllic, propylitic and gossan in RGB of W. Fatirah area, NED, Egypt

in all rock units except younger gabbros and monzogranites. Color composite image of the three ratios [(5+7)/6, (7+9)/8 and (4/2)] in RGB, representing phyllic, propylitic alteration and gossan respectively, was created to enhance and facilitate the visual interpretation (Fig. 13). In this way, alteration mineral assemblage can be identified through different colors. Phyllic alteration zones manifested as light magenta color, propylitic alteration zones as the green color and finally the areas that rich in gossan manifested as blue and violet colors.

Principal component analysis (PCA)

The principal component analysis (PCA)-transformation for the seven reflected Landsat-8 bands of the studied area has been calculated with their Eigenvector values as listed in (Table. 1). PC1 concentrates common features to all input bands (usually topography) and often displays important structural information. PC2 is orthogonal to PC1 in n directional space and highlights the spectral differences between visible and the infrared spectral bands. PC3 includes the third most variable component that is orthogonal to the other two PCs. The first three pcs (PC1, PC2 and PC3 in RGB) are combined (Fig. 14). The image highlights the subtle differences between the rock units especially the metavolcanics, younger gabbros and younger granites.

A Feature-Oriented Principle Components Selection (FPCS) was applied to the ASTER VNIR-SWIR bands in order to delineate four hydrothermal alteration minerals. The ASTER bands 1, 2, 5, and 8 are chosen taking into account the spectral characteristics of chlorite. Chlorite has high reflectance values in ASTER bands 1 and 5 and strong absorption values in bands 2 and 8. Applying these selected bands in a principal component analysis revealed four PCs, the resulting Eigenvectors statistics are summarized in (Table 2).

Table.1: Eigenvector values of principal component analysis (PCA) of the seven reflected Landsat-8 bands of W. Fatirah area, NED, Egypt

PC	Band 1	Band 2	Band 3	Band 4	Band 5	Band 6	Band 7	Eigen value%
PC1	-0.180	-0.203	-0.293	-0.398	-0.437	-0.507	-0.483	96.45
PC2	0.318	0.321	0.376	0.379	0.212	0.474	-0.489	2.95
PC3	-0.389	-0.406	-0.314	0.249	0.648	0.030	-0.317	0.41
PC4	-0.079	-0.070	-0.093	0.049	0.196	0.717	0.651	0.187
PC5	-0.302	-0.249	0.099	0.731	-0.545	0.005	0.052	0.035
PC6	-0.665	0.077	0.681	-0.280	0.082	0.028	-0.011	0.016
PC7	-0.415	0.785	-0.435	0.135	-0.028	0.015	-0.013	0

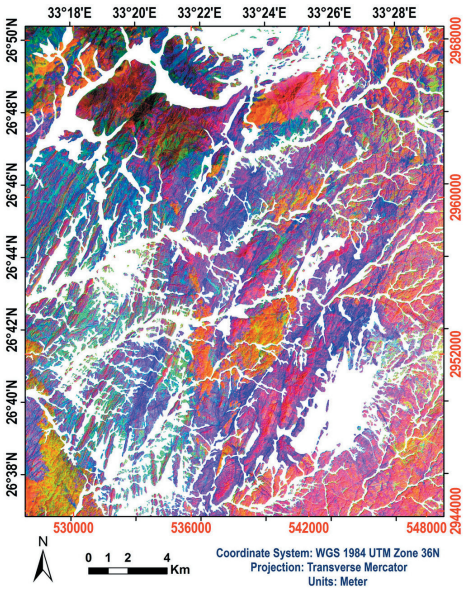

Fig. 14: PCA color composite of PC1, PC2 and PC3 in RGB of W. Fatirah area, NED, Egypt

PC3 has high loading for band 5 (negative loading -0.662) and band 8 (positive loading 0.684). Hence, chlorite will appear in bright pixels. The threshold process was carried out on PC3 to exclude chlorite of low concentration values. The threshold of chlorite was calculated as:

Band DN threshold = Mean + 2 (Standard Deviation) = 80.53 + (2×86.96) = 254.45

The resulting image (Fig. 15) shows chlorite alteration areas that exceed the threshold value as a pale green color.

The ASTER bands 1, 4, 6, and 7 are chosen taking into account the spectral characteristics of kaolinite. The main reason for this selection is that the kaolinite has the highest reflectance values in bands 4, 7 and high absorption features in bands 1 and 6. The results of principal components analysis of these selected bands revealed four PCs, the resulting Eigenvectors statistics are summarized in (Table.3).

Table. 2: Eigenvector statistics for ASTER bands 1, 2, 5, and 8 of W. Fatirah area, NED, Egypt

PC	Band 1	Band 2	Band 5	Band 8	Eigenvalue	Eigen %
PC1	0.487	0.487	0.521	0.502	27265.82	97.9%
PC2	0.545	0.477	-0.504	-0.469	476.28	1.71%
PC3	-0.215	0.218	-0.662	0.684	78.83	0.283%
PC4	0.646	-0.697	-0.188	0.243	23.84	0.09%

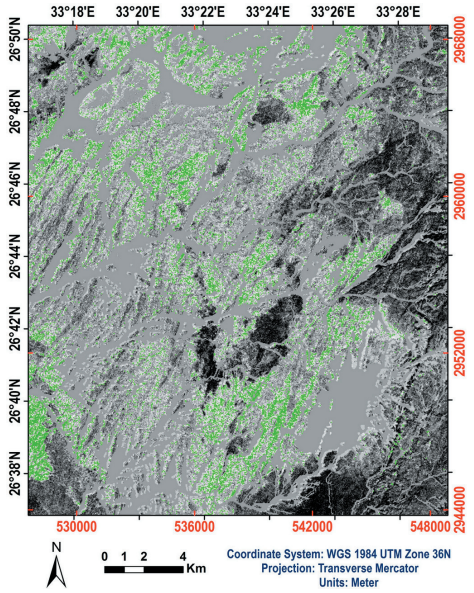

Fig.15 : Resulted image for chlorite produced by Crosta technique,*(pale green color is the expected threshold anomalies at 95% confidence)*

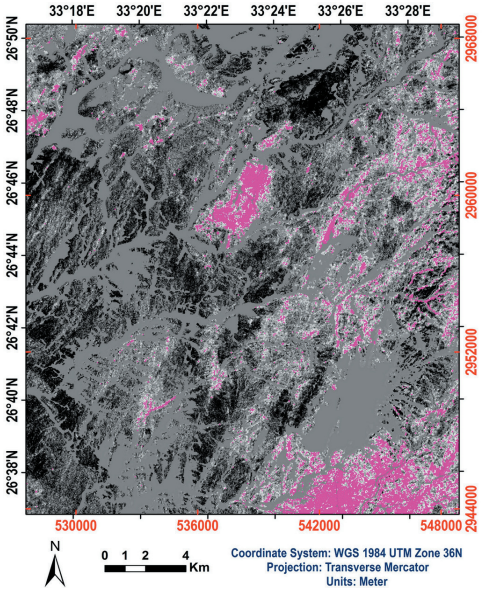

Fig. 16: Resulted image for kaolinite produced by Crosta technique, *(purple coloris the expected threshold anomalies at 95% confidence)*

Table. 3: Eigenvector statistics for ASTER bands 1, 4, 6, and 7 of W. Fatirah area, NED, Egypt

PC	Band 1	Band 4	Band 6	Band 7	Eigenvalue	Eigen %
PC1	**0.474**	**0.506**	**0.510**	**0.506**	**28176.81**	**98%**
PC2	**0.876**	**-0.232**	**-0.241**	**-0.345**	**377.73**	**1.32%**
PC3	**0.026**	**-0.805**	**0.548**	**0.227**	**65.272**	**0.228%**
PC4	**-0.074**	**0.203**	**0.617**	**-0.756**	**47.168**	**0.165%**

PC3 has high loading for band 4 (negative loading = -0.805) and band 6 (positive loading = 0.548). Therefore, PC3 was subjected to a mathematical negation, then kaolinite appears in bright pixels. The threshold process was carried out on PC3 to exclude kaolinite of low concentration values. The threshold of kaolinite was calculated band DN threshold = 251.39. The resulting image (Fig. 16) shows kaolinite alteration areas that exceed the threshold value as purple color.

The ASTER bands 1, 3, 5, and 6 are chosen taking into account the spectral characteristics of illite. Illite has high reflectance features in band 1 and 5 and strong absorption in band 3 and 6. The results of principal components analysis of these selected bands revealed four PCs where the resulting Eigenvectors statistics are summarized in (Table.4).

PC3 has high loading for band 1 (positive loading = 0.648) and band 3 (negative loading = -0.701). So, PC3 was subjected to a

Table. 4: Eigenvector statistics for ASTER bands 1, 3, 5, and 6 of W. Fatirah area, NED, Egypt

PC	Band 1	Band 3	Band 5	Band 6	Eigenvalue	Eigen %
PC1	0.481	0.492	0.515	0.510	27982.65	98.01%
PC2	0.561	0.462	-0.507	-0.462	460.05	1.163%
PC3	0.648	-0.701	0.240	-0.177	50.356	0.177%
PC4	0.182	-0.230	-0.647	0.703	29.589	0.104%

mathematical negation, then illite appears in bright pixels. The threshold process was carried out on PC3 to exclude illite of low concentration values. The threshold of illite was calculated band DN threshold = 254.4. The resulting image (Fig. 17) shows illite alteration areas that exceed the threshold value as a yellow color.

The ASTER bands 3, 5, 6, and 8 are chosen taking into consideration the spectral characteristics of hematite. Hematite has high reflectance features in band 5 and 8 and strong absorption in band 3 and 6. The results of principal components analysis of these selected bands revealed four PCs and the resulting Eigenvectors statistics are summarized in (Table. 5).

PC3 has high loading for band 5 (positive loading = 0.589) and band 8 (negative loading = -0.797). So that PC3 was subjected to a mathematical negation, then hematite appears in bright pixels. The threshold process was carried out on PC3 to exclude hematite of low concentration values. The threshold of hematite was calculated band DN thresh-

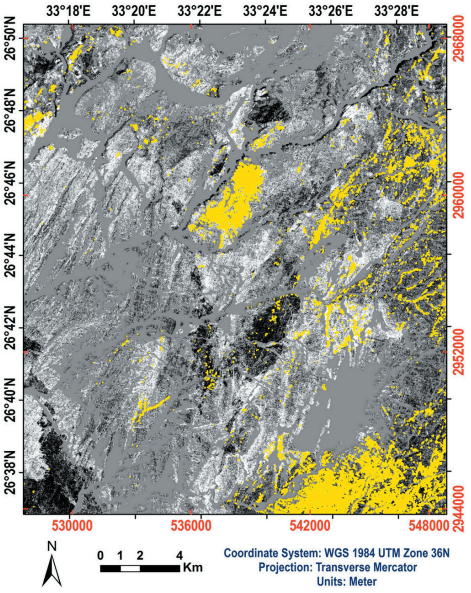

Fig. 17: Resulted image for illite produced by Crosta technique, *(yellow color is the expected threshold anomalies at 95% confidence)*

Table.5: Eigenvector statistics for ASTER bands 3, 5, 6, and 8 of W. Fatirah area, NED, Egypt

PC	Band 3	Band 5	Band 6	Band 8	Eigenvalue	Eigen %
PC1	-0.483	-0.512	-0.508	-0.494	28516.48	98.6%
PC2	-0.870	0.349	0.292	0.188	302.087	1.045%
PC3	0.094	0.589	0.091	-0.797	72.173	0.25%
PC4	0.0001	-0.517	-0.804	0.290	25.685	0.089%

old = 251.39. The resulting image (Fig. 18) shows hematite alteration areas that exceed the threshold values as red color.

Airborne Gamma-Ray Spectrometry

The airborne gamma-ray spectrometric data of the study area were processed and treated qualitatively and quantitatively. The qualitative interpretations result in three radioelements maps as well as one ternary map whereas the quantitative treatment used to clarify the radioelements contents of each rock unit.

Qualitative interpretation of the airborne gamma-ray spectrometric data

Radioelements contour maps comprising (eU in ppm), (eTh in ppm) and (K %) are shown in (Figs. 19-21) respectively where the measured values are multiplied by 10 to exaggerate the difference between the different

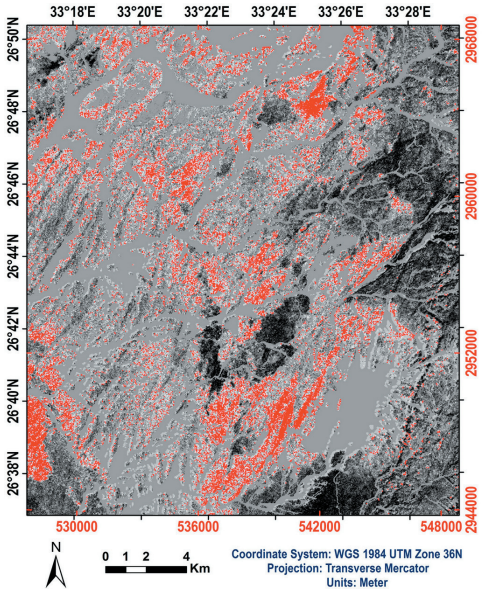

Fig. 18: Resulted image for hematite produced by Crosta technique, *(red coloris the expected threshold anomalies at 95% confidence)*

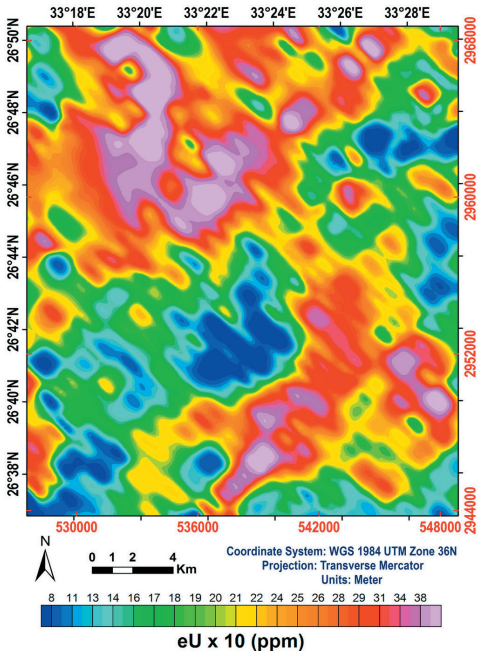

Fig. 19: Airborne (eU in ppm) radiometric contour map of W. Fatirah area, NED, Egypt

rock units. The interpretation of radioelements distribution for mapping the surface geology is because each rock type has its own rock-forming minerals with certain amounts, which comprise specific quantities of radioactive elements (Elawadi, et al., 2004). The radioelements concentration can attribute either to hypogene and supergene enrichment. The higher degree of weathering may produce a distinctive gamma-ray response compared with the surrounding bedrock (Wilford, 1992). The concentration of eU , eTh and K could be classified into three levels. The younger granites, the Dokhan volcanics, and the older granitoids have the highest levels (red to magenta colors) with concentration (29 to 38 ppm, 81 to 124 ppm and 28 to 31%) for eU, eTh, and K respectively. The intermediate level (yellow to pale orange colors) with concentration (22 to 27 ppm, 64 to 79 ppm and 23 to 27%) for eU, eTh, and K respectively, which mainly associated with

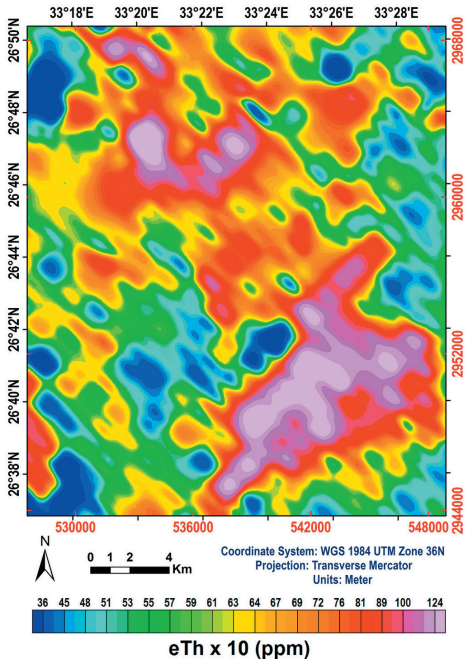

Fig. 20: Airborne (eTh in ppm) radiometric contour map of W. Fatirah area, NED, Egypt

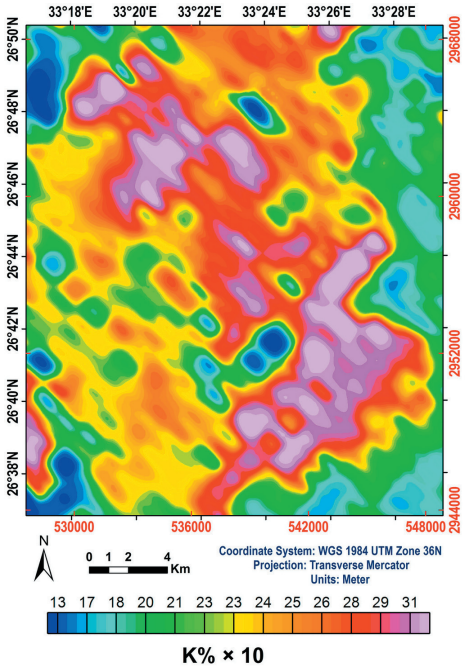

Fig. 21: Airborne (K %) radiometric contour map of W. Fatirah area, NED, Egypt

older granitoids and some parts of younger granites (monzogranites). The metavolcanics and the younger gabbros exhibit the lowest levels (blue to green colors) of eU, eTh and K (6 to 19 ppm, 34 to 60 ppm and 11 to 20%), respectively.

Ternary maps are composite images that provide a simultaneous display of up to three parameters on one image and facilitates the correlation and delineation of areas based on subtle differences in the numerical values. In this case, the additive primary colors, red, green and blue (RGB) are used. The intensity of each color depends on the concentration of the radioelement. Black color represents the low concentrations of all three elements while white color reflects the high ones. These composite ternary maps are developed by the USGS (Duval, 1983). The ternary map of eU, eTh and K in RGB respectively (Fig. 22) revealed that the maximum concentration of the radioelements is associated with younger granites (syenogranites and alkali feldspar granites).

Quantitative interpretation of the airborne gamma-ray spectrometric data

The average equivalent uranium (eU) and equivalent thorium (eTh) abundances in felsic intrusive and extrusive rocks such as granites and rhyolites are 4.5 and 15.7 ppm, respectively (Boyle, 1982). The minimum, maximum and average of the eU (ppm), eTh (ppm) and K multiplied by 10 as well as their eTh/eU ratio of each rock unit cropped out in the study area are shown in (Table.6) and (Fig. 23). It is clear that the metavolcanics show the lowest eU, eTh and K contents as well as eTh/eU ratio. From this table, the metavolcanics have eU average 16.9 ppm and eTh av-

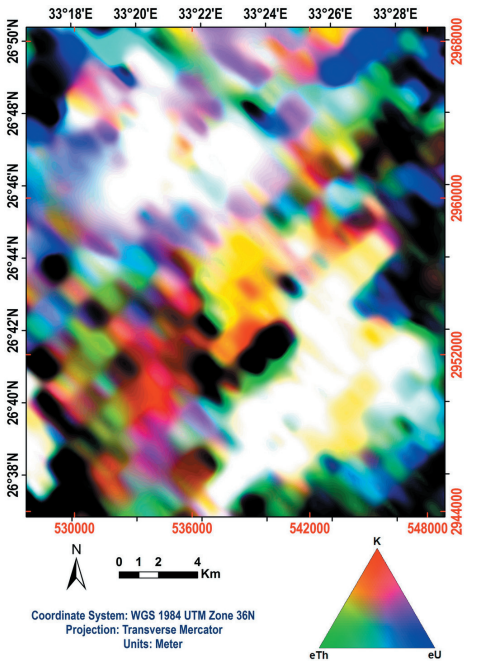

Fig. 22: Radioelements composite image (eU, eTh, K and eU in RGB) of W. Fatirah area, NED, Egypt

an average of 5.99. It is clear that the average contents of the radioelements distributed in the younger granites mostly within the normal range. They have eU average 24.08 and eTh average 81.39. The eTh/eU ratio with an average of 3.01 to 3.73 in Syenogranites.

Laboratory spectrometric measurements

Forty samples representing the different rock units exposed in the studied area were radiometrically analyzed for uranium- and thorium-contents. The eU, eTh contents in ppm and K% of these rocks as well as their eTh/eU ratio are listed in (Table. 6) and (Fig. 24). It is quite clear from the table that the granitic rocks (older granitoids and younger granites) have eU contents ranging from 1 to 15 ppm with the highest average 8.107 ppm and eTh contents from 3.4 to 24.2 ppm with highest average 15.725 ppm in syenogranites. The eTh/eU ratio ranges from 1 to 6.9 with the highest average of 3.27 in monzogranites. The metavolcanics have a higher value of eTh/eU ratio (3.18) than the Dokhan volcanics.

Table 6: Airborne Gamma-Ray and laboratory spectrometric data of eU, eTh, K and eTh/eU ratio of the different rocks at W. Fatirah area, NED, Egypt

Rock type		Airborne spectrometry (ppm)* (values multiplied by 10)				Laboratory measurements (ppm) **			
		eU (ppm)	eTh (ppm)	K %	eTh/eU	eU (ppm)	eTh (ppm)	K %	eTh/eU
Alkali Feldspar Granites N* = 249 N** = 7	Minimum	6.47	46.88	12.53	1.07	2.4	9.4	3	1.5
	Maximum	44.26	89.17	32.67	11.22	10.9	17.4	3.9	6
	Average	22.93	67.52	26.37	3.73	5.428	12.8	3.5	2.78
Syenogranites N* = 2105 N** = 8	Minimum	1.72	23.00	8.58	1.15	2.3	9.7	3	1
	Maximum	49.18	150.27	37.25	28.96	15	24.2	3.7	4.1
	Average	24.08	81.39	26.72	3.71	8.107	15.725	3.31	2.23
Monzogranites N* = 1954 N** = 4	Minimum	6.73	23.46	8.79	1.45	1.3	6.2	2.2	1.7
	Maximum	46.53	112.2	33.61	7.11	6	11.4	4	4.6
	Average	21.91	61.08	23.43	3.01	3.5	9.7	2.85	3.27
Younger Gabbros N* = 218 N** = 5	Minimum	2.03	16.62	7.31	2.32	1.2	3	0.5	0.9
	Maximum	24.91	85.92	29.39	17.06	3.5	5.7	1.1	3.3
	Average	10.07	50.02	19.02	5.99	2.54	4.12	0.82	1.84
Dokhan Volcanics N* = 946 N** = 3	Minimum	7.93	32.45	8.9	1.09	1.2	3.6	2.3	1.4
	Maximum	77.76	167.6	35.56	5.02	3.3	5	2.8	2.9
	Average	29.86	76.04	24.95	2.65	2.3333	4.466	2.56	2.07
Older Granitoids N* = 2839 N** = 10	Minimum	2.85	21.64	12.9	0.48	1	3.4	1.1	1.4
	Maximum	59.01	152.51	35.35	17.91	7.2	10.6	3.2	6.9
	Average	20.25	62.97	20.54	3.37	3.84	8.14	2.41	2.61
Metavolcanics N*= 468 N** = 6	Minimum	0.53	19.24	4.73	1.16	0.3	3.5	0.8	0.5
	Maximum	46.7	96.34	31.13	43.39	6.9	5.9	3.1	11.8
	Average	16.9	45.67	15.74	3.36	3.016	4.25	1.4	3.18

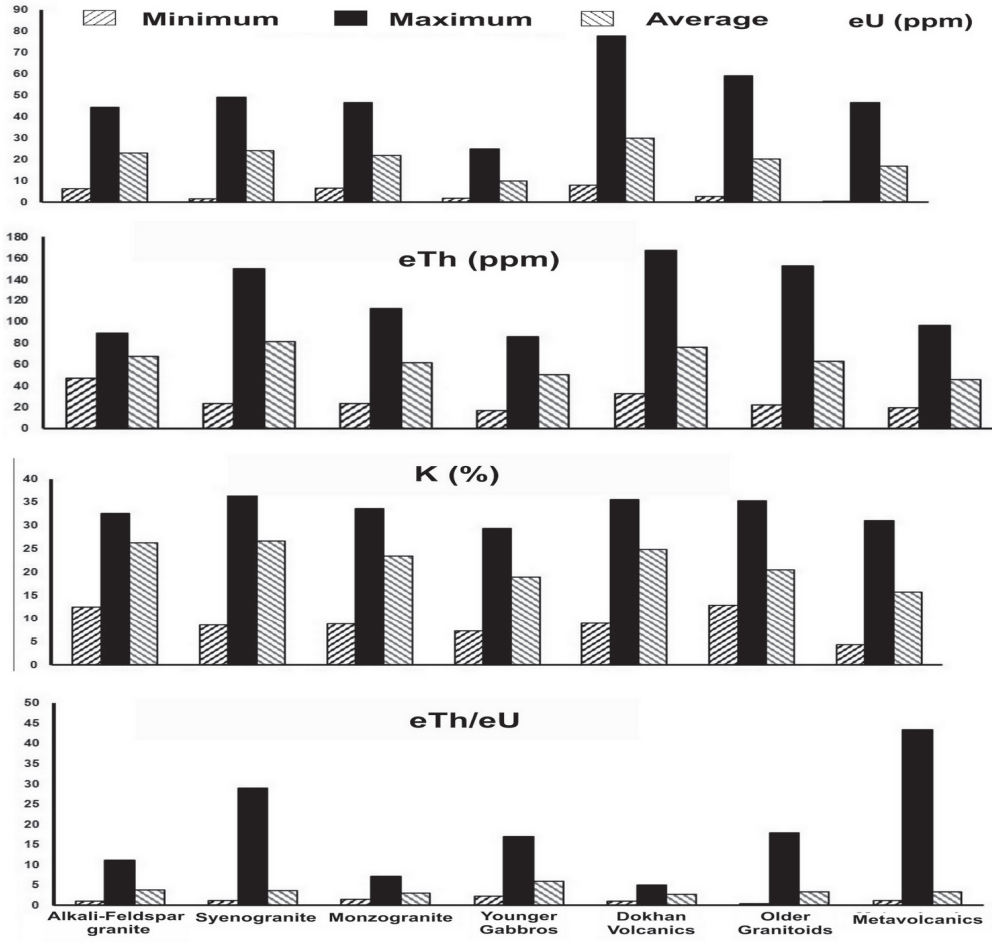

Fig. 23: Bar diagrams showing the minimum, maximum and averages (mulytiblied by 10) of Airborne eU, eTh, K and eTh/eU in the different rocks of W. Fatirah area, NED, Egypt

erage 45.67 ppm. The eTh/eU ratio ranges from 1.16 to 43.39 with an average of 3.36. The older granitoids have eU average 20.25 ppm and eTh with an average 62.97 ppm. The eTh/eU ratio ranges from 0.48 to 17.91 with an average of 3.37. The Dokhan volcanics have eU average 29.86 ppm and eTh with an average 76.04 ppm. The eTh/eU ratio ranges from 1.09 to 5.02 with an average of 2.65. The younger gabbros have eU average 10.07 ppm and eTh with an average 50.02 ppm. The eTh/eU ratio ranges from 2.32 to 17.06 with

Field work Verification

More than one hundred ground truth areas were checked and verified in the field. Based on the fieldwork investigations, remote sensing processed data products of Landsat-8 and ASTER, spatial distribution as well as radio-elements distribution maps and contact relationships, the main rock units of the study area are represented by metavolcanics, older granitoids, Dokhan volcanics, younger gabbros, younger granites, post granitic dikes and

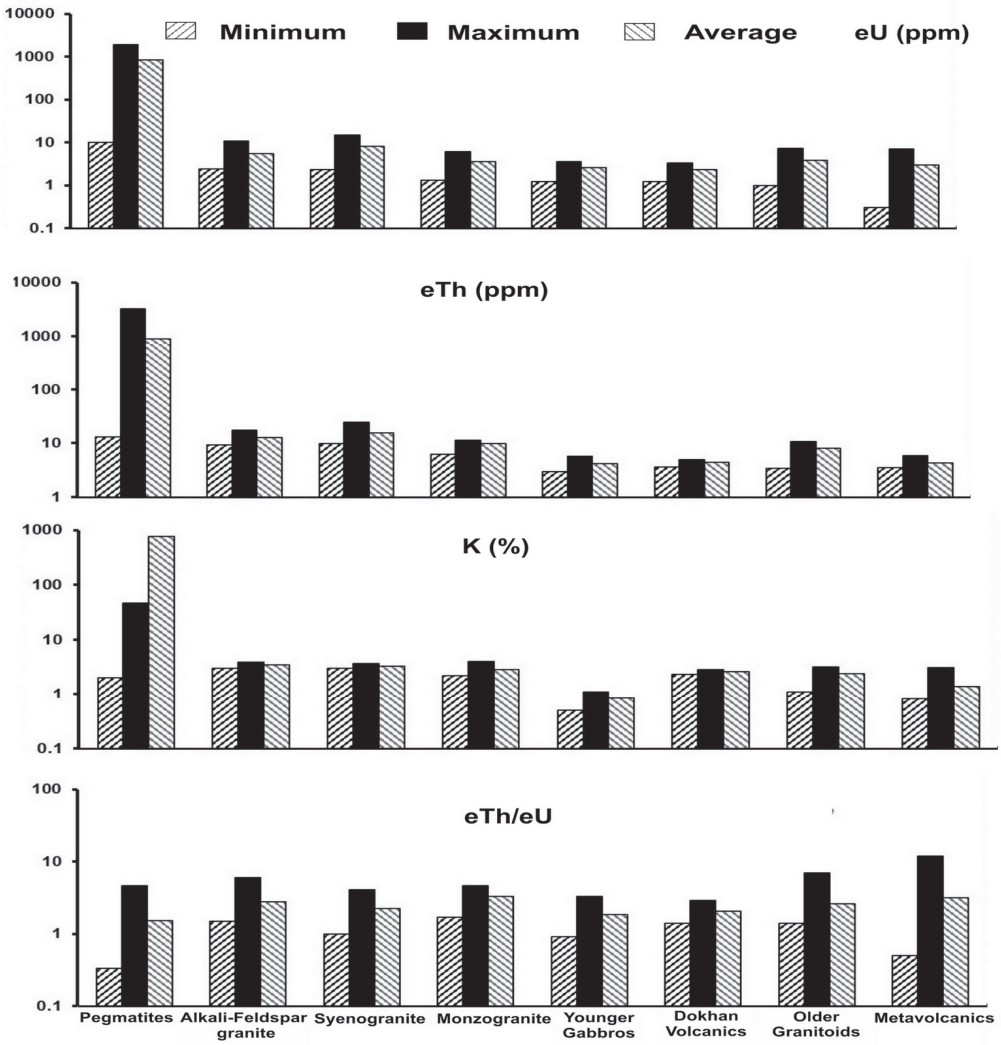

Fig. 24: Bar diagrams showing the minimum, maximum and average contents of Laboratory eU, eTh and K as well as the eTh/eU ratios of the different rocks of W. Fatirah area, NED, Egypt

pegmatites.

The metavolcanics represent the oldest rock unit in the studied area. They show moderate to high topography and cropping out, in the western and northern parts of the map, as belts extending in the NE-SW direction that extends westwards beyond the western limits of the studied area. The metavolcanics are actually represented by the island arc association. The metavolcanics are highly altered in some areas especially that in contact with the older granitoids and the younger granites. They are mineralized with iron in the forms of (BIF and ochre) at W. Fatirah El-Zarqah. The studied island arc association (YMV of Stern, 1979) is represented mainly by metabasalts, meta-andesites and their metapyroclas-

tics. The metapyroclastics are the dominant rock type, which varies in grain size from ash- to agglomerate and most of them are banded. At W. Fatirah El-Zarqah and W. Abu Zawal. The metavolcanics are capped with lamination and banding of the Dokhan volcanics, which show typical columnar jointing at their top parts. Mostly, the metapyroclastics show different attitudes, vertical at the southern side of W. Abu Zawal (Fig. 25). The banding also varies in thickness, from few meters to few millimeters and in color due to the difference in mineral composition**.** The very fine-grained banded and welded tuffs are the most common type of these metapyroclastics and mainly composed of ashes and dust. In addition, there are metavolcanic xenoliths, which appearing frequently in younger granites. Generally, the metavolcanics are dissected by mafic to felsic dikes of different attitudes from steeply dipping to gently dipping ones.

Fig. 25: Fine-grained banded tuffs with nearly vertical attitude, W. Abu Zawal, notice Felsic dike is conformable

The older granitoids are characterized by the general low topography. In some areas, they exhibit a gneissic structure. They are medium-to coarse-grained containing numerous amounts of mafic minerals. Sometimes, they attain high topography forming mountainous bodies with well-developed semi-rounded boulders (Fig. 26) that quarried as building stones especially at the eastern part of G. El-Urf. The older granitoids intrude the metavolcanics at W. Abu Shihat and include several differently-sized and -shaped xenoliths. They are in turn intruded by the younger gabbros and the younger granites where the latter two intrusions contain numerous xenoliths from them as well as roof-pendants. The older granitoids are characterized by the common presence of feldspar pockets and veins that mined for feldspars especially at G. El-Urf. Locally, the color of the older granitoids becomes lighter due to quartz injection near the contact with the younger granites where most of the fractures and joints are stained with limonitic iron oxides.

Fig. 26: Bouldery appearance in older granitoids (OGR) east G. El-Urf

Abu Zeid (1991) stated that the Dokhan volcanics evolved in a subduction-related volcanic arc environment on a crustal thickness intermediate between an island arc and an active continental margin setting during the final stages of the late Precambrian Pan-African orogeny in Egypt. El-Sharkawy et al. (1991) studied the volcanic rocks of G. Dokhan and stated that these volcanics are regarded as the type locality for one volcanic succession "Dokhan volcanics". The studied Dokhan volcanics occupy one elongated belt (G. Fatirah) which extend further north beyond the northern limit of the mapped area. They are of grey color with moderate to high topography and composed mainly of intermediate rocks and intruded by the monzogranites, sy-

enogranites as well as alkali-feldspar granites at W. Fatirah El-Beidah, W. Fatirah El-Zarqah and W. Abu Kharif. Their contact with the younger granites is sharp and dips away from the granitic intrusion. They cap the older granitoids of W. Abu Kharif. The Dokhan volcanics in the studied area are distinguished into intermediate to rather felsic volcanic rocks that consist mainly of andesites and dacites (Fig. 27).

The younger gabbros are exposed in two outcrops, the first outcrop is traversed by W. Abu Zawal and the second one is at south W. Abu Shihat. They are characterized by their low to moderate topography and their blocky appearance. The younger gabbros are intruded by the syenogranites (Fig. 28) of G. El-Urf as well as the monzogranites of W. Abu Zawal with characteristic offshoots and apophyses where the contact in between is sharp and dips away from the granite intrusion. On the other hand, they intrude both the metavolcanics and the older granitoids as fingers and carry them as roof pendants especially at the western part of W. Abu Shihat. Generally, the younger gabbros of W. Fatirah area are characterized by their greenish-grey to dark grey color and medium to coarse grain size.

The younger granites are represented by three main types namely; Monzogranite, Syenogranite and Alkali-feldspar granite with alkaline granites. The younger granites are widely distributed all over the Egyptian Precambrian shield constituting approximately 30% of its plutonic assemblage (El-Gaby et al., 1988). They are classified as Gattarian granites (Hume, 1935), red and pink granites (Akaad and El-Ramly, 1961), late- and post-orogenic granites (El Shazly, 1964) and G-II and G-III granites (Hussein et al., 1982). It is believed that, these granites have been formed about 575 to 600 m.y. and may represent the last major tectonic magmatic event in the evolution of the crystalline shield of the Egyptian Eastern Desert (Rogers and Greenberg, 1983).

Fig. 27: Dokhan volcanics (DV) of intermediate composition with Dacite in G. Fatirah

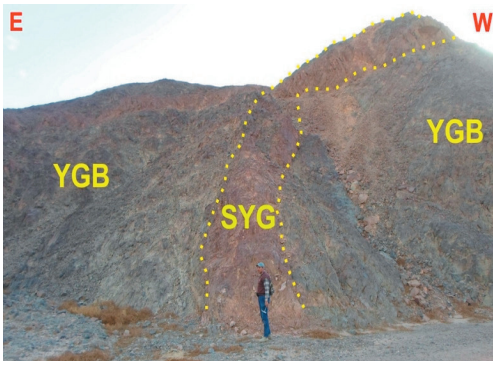

Fig. 28: Syenogranite offshoot (SYG) cutting the younger gabbros (YGB), W. Abu Zawal

The monzogranites crop out around the western parts of W. Fatirah El-Beidah and W. Abu Zawal. They intrude the older granitoids and the metavolcanics. The contact with the older granitoids is gradational where hybrid zone, was produced and roof-pendant from the older granitoids was observed On the other hand, the contact with the metavolcanics is sharp and dips away from the granite intrusion. Monzogranite is characterized by its low topography, bouldery appearance, and spheroidal exfoliation, presence of xenoliths either from metavolcanics or from older granitoids. They are traversed by several wadis such as W. Fatirah El-Beidah, W. Fatirah El-Zarqah

and W. Abu Zawal and attain a moderate topography near the contact with the syenogranite. It is medium-to coarse-grained with some feldspar phenocrysts.

The syenogranites represent the dominant type of younger granites in the area. It is characterized by medium-to coarse-grained, pink in color, moderate to high topography, which forms the summits of G. El-Urf as well as the area around G. El-Dob and the masses of W. Fatirah El-Beidah. They have dike-like appearance and are characterized by the presence of vertical and horizontal well-developed joint sets. They are characterized by its high to moderate topography and the common presence of roof-pendants of metavolcanics (Fig. 29), older granitoids, Dokhan volcanics, younger gabbros and monzogranites. It is pink in color, medium- to coarse-grained and characterized by the common presence of more than one set of joints and several xenoliths of the older rocks ranging in size from few centimeters to few meters besides roof-pendants.

The alkali feldspar granites crop out as sporadic masses in the central and northeastern parts of the study area representing the last phase of the younger granites and they are characterized by a yellowish pink color, very high topography, semi-rounded mountainous masses and well represented in G. El-Dob, G. Abu Kharif and G. Abu Hamr. They are occupying elliptical to semi-rounded masses of alkaline granite and intrude the surrounded rock units (Fig. 30). These granitic rocks are characterized by blocky appearance, presence of numerous xenoliths of the older rocks and absence of exfoliation and cavernous weathering.

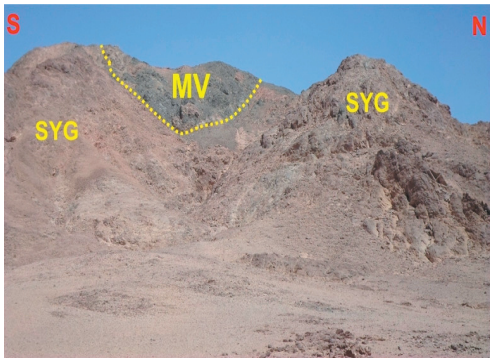

Fig. 29: Metvolcanics (MV) roof pendant is upon the syenogranites (SYG), W. Fatirah El Zarqah

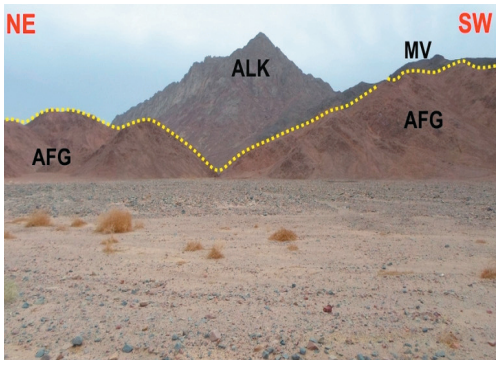

Fig. 30: G. Abu Kharif alkaline granite (ALK) intruding the alkali-feldspar granite (AFG) which in turn carries metavolcanics (MV) as roof pendants, W. Abu Kharif.

Petrographic Investigations

Petrographically, the Metavolcanics are represented by porphyritic metabasalts, meta-andesite and their metapyroclastics, which are represented mainly by lithic meta-tuffs. The porphyritic metabasalts are generally fine-grained and show porphyritic texture with plagioclase. They consist of microphenocrysts of plagioclase and hornblende embedded in a finer holocrystalline groundmass of plagioclase, hornblende, opaques and sphene. In some samples, relics of augite were observed. Zoisite, sericite, kaolinite, calcite, epidote and chlorite are secondary minerals, a feature confirmed that these rocks are metamorphosed up to the greenschist facies. However, primary magmatic features, such as minerals and textures, are still preserved. The meta-andesites are fine-grained, porphyritic and composed mainly of plagioclase and hornblende phenocrysts set in a groundmass having the same

composition. The main accessory minerals are apatite, sphene, zircon and opaques. Chlorite, epidote, and kaolinite are secondary minerals. The groundmass is composed of microlites and short laths of plagioclase, hornblende, chlorite, opaques and sphene. The metapyroclastics are represented mainly by lithic meta-tuffs that are predominantly composed of lithic fragments as well as subordinate amounts of crystal fragments. The crystal fragments recorded are plagioclase, quartz and hornblende. Opaques and apatite are accessory minerals whereas epidote and chlorite are secondary minerals. The lithic fragments comprise mainly basaltic and andesitic fragments as well as reworked tuffs.

The older granitoids range in composition from quartz-diorite through tonalite to granodiorite. Quartz-diorites are medium- to coarse-grained, holocrystalline and hypidiomorphic and composed essentially of plagioclase, quartz, biotite, hornblende and minor alkali feldspars. Sphene (Fig. 31), zircon, apatite and opaques are accessory minerals. Epidote, chlorite, sericite, and kaolinite are secondary minerals. In some samples, the gneissic texture is observed. Granodiorite is coarse-grained and exhibiting hypidiomorphic granular texture. It is composed mainly of plagioclase and quartz together with subordinate alkali feldspars, biotite and hornblende. Opaques, zircon, apatite and sphene are accessory minerals whereas chlorite, sericite, and kaolinite, are secondary minerals.

The Dokhan volcanics are represented by andesites (porphyritic and non-porphyritic), trachy-andesite and dacites as well as their equivalent pyroclastic, which are mainly represented by crystal lithic tuffs. Porphyritic andesites are the dominant rock variety. They are fine-grained, porphyritic and of greenish-grey color and mainly composed of plagioclase and hornblende with the subordinate amount of quartz. Zircon, apatite and opaques are the main accessory minerals whereas epidote, chlorite and sericite are secondary minerals. The andesites show, generally, phenocrysts set in a finer microcrystalline groundmass. Sometimes, they exhibit glomeroporphyritic as well as pilotaxitic texture without phenocrysts but they are less abundant. The plagioclase phenocrysts are generally oriented in a sub-parallel manner (Fig. 32). Trachy-andesite occurs in a minor amount as a variety similar the porphyritic andesite but has a trachytic texture and contain alkali feldspar with plagioclase. The plagioclase laths in the groundmass become coarser and arranged in a sub-parallel manner exhibiting trachytic texture and they are intensively sericitized. Dacites are less dominant than andesites. They are porphyritic and composed mainly of pla-

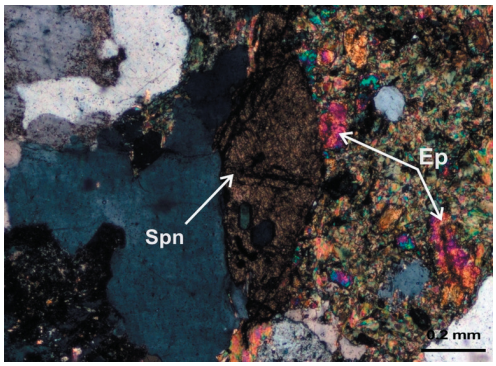

Fig. 31: Epidotization (Ep), muscovitization, sphene (Spn) in quartz diorite, XPL

Fig. 32: Lamellar twinning in subparallel plagioclase (Pl) phenocrysts in porphyritic andesite, Dokhan volcanics, XPL

gioclase, quartz, alkali feldspars and biotite phenocrysts set in a cryptocrystalline fine-grained groundmass composed of the same components (Fig. 33). Opaques, zircon, apatite, and sphene are accessories while sericite and chlorites are secondary minerals. Crystal lithic tuffs are medium-grained and made up of both crystal and lithic fragments that are imbedded in tuffaceous matrix. The crystal fragments are represented by plagioclase and quartz whereas the lithic fragments are of andesitic and dacitic composition. Andesitic lithic fragments consist of plagioclase and intensively chloritized hornblende. The dacitic fragments are composed of plagioclase, quartz and chloritized biotite set in a fine-grained groundmass of the same constituents. Apatite and opaques represent the accessory minerals whereas chlorite, epidote and sericite are the secondary minerals.

Detailed petrographic studies as well as the field relations and observations showed that the younger gabbros are represented by mesogabbros and leucogabbros, which are belonging to the other intrusive younger gabbros of the Eastern Desert and Sinai (Takla et al., 1981 and El-Gaby et al., 1988). The mesogabbros which are the dominant type of younger gabbros are medium- to coarse-grained, mesocumulate and exhibiting hypidiomorphic granular texture. They are composed of plagioclase, augite, oxyhornblende and opaques. Chlorite and saussurite are alteration products. Leucogabbros are less abundant in the investigated area than the mesogabbros. They are coarse-grained, equigranular, hypidiomorphic and composed of plagioclase, pyroxene, hornblende, and opaques. They are adcumulate rocks in which unzoned plagioclase crystals exhibiting adcumulus texture and entrap between them intercumulus pyroxene.

The younger granites are represented by monzogranite, syenogranite and alkali-feldspar granite with alkaline granites. Monzogranites are coarse-grained, holocrystalline and showing seriate porphyritic and granitic textures at the margin and the core of the plutons respectively. They consist essentially of quartz, perthite, plagioclase (Fig.34), hornblende as well as biotite. Opaques, sphene, apatite, and zircon are accessory minerals. Kaolinite, sericite, chlorite and epidote represent secondary minerals. Syenogranites are holocrystalline, showing hypidiomorphic granular texture and consisting mainly of perthite (orthoclase and microcline), quartz, plagioclase and a minor amount of biotite and/or muscovite in decreasing order of abundance. This rock unit differs from the monzogranite by increasing the alkali feldspar content and has no hornblende, lesser

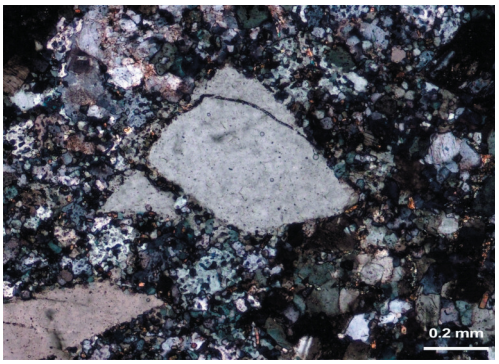

Fig. 33: General view of dacite showing alkali feldspar phenocrysts in fine-grained groundmass, Dokhan volcanics, XPL

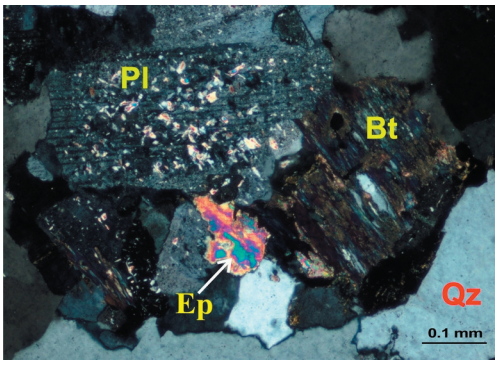

Fig. 34: General view of monzogranite showing sericitized plagioclase, chloritized biotite (Bi), quartz (Qz) and epidote (Ep), XPL

biotite, and opaque. Zircon, fluorite, apatite, cassiterite, sphene and opaques are accessory minerals, whereas chlorite, kaolinite, sericite, epidote and sphene represent the secondary minerals (Fig.35). Alkaline granites are represented by riebeckite granites. These rocks are holocrystalline, medium- to coarse-grained and showing hypidiomorphic granular texture. They are composed of alkali feldspars, quartz, riebeckite, biotite and a very little amount of plagioclase. Zircon, apatite, allanite (Fig. 36) and opaques are accessory minerals whereas chlorite, sericite, sphene and kaolinite are secondary minerals.

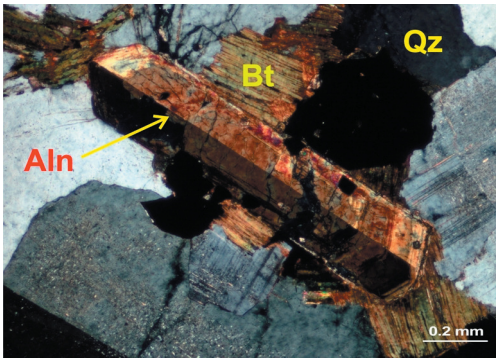

Fig. 36: Twinned and zoned prismatic allanite (Aln) crystal in alkali-feldspar granite, XPL

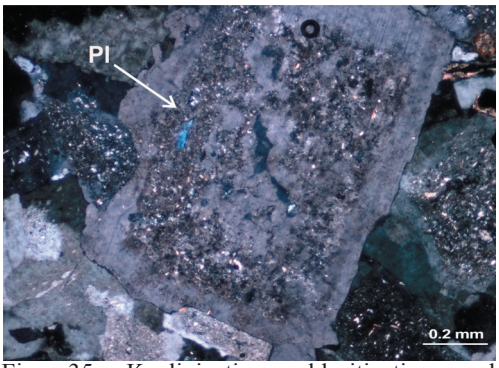

Fig. 35: Kaolinization, chloritization and sericitization in syenogranites, XPL

This rock type differs from the previous syenogranites in increasing of the alkali feldspar (represented only by orthoclase perthite) contents (70-80 % of the rock), presence of riebeckite and absence of muscovite.

CONCLUSIONS

The integrated methods used in this study including Landsat-8 and ASTER images as well as the airborne radioelements processing followed by field investigations and detailed petrographic study resulted in a geological map (Fig. 37) with an accuracy 88.2 % with a kappa coefficient value of 0.825, the used integrated methods have shown the compatibility of the results for the rock units discrimination and their radioactive potentiality through locating the anomalous radioactive zones. This reflects the need for using multiple ways and methods to obtain confirmatory data and qualified results.

The spectral analysis of Landsat-8 and ASTER data at W. Fatirah area revealed results prove the great capability of remote sensing techniques in geological mapping and discriminate hydrothermal alteration minerals. Two false-color composite images of Landsat-8 bands (b7, b5, b3 in RGB) and ASTER bands (b7, b4, b2 in RGB) facilitate the visual interpretation of the lithological units. Detecting of areas rich in iron oxides, ferromagnesian minerals and OH-bearing minerals at 95% confidence achieved utilizing three landsat-8 band ratios (b4/b2, b5/b6 and b6/b7) respectively. Moreover, their color combination in RGB revealed that the younger granites in the study area could be distinguished in three verities and differentiate between the metavolcanics and their pyroclastic that composed of tuffs and agglomerates.

Alteration mineral assemblage (propylitic, phyllic in addition to gossan) delineated through ASTER band ratios (b7+b9)/b8, (b5+b7)/b6 and b4/b2 respectively and their color combination in RGB. The images revealed that A) propylitic alteration zones are

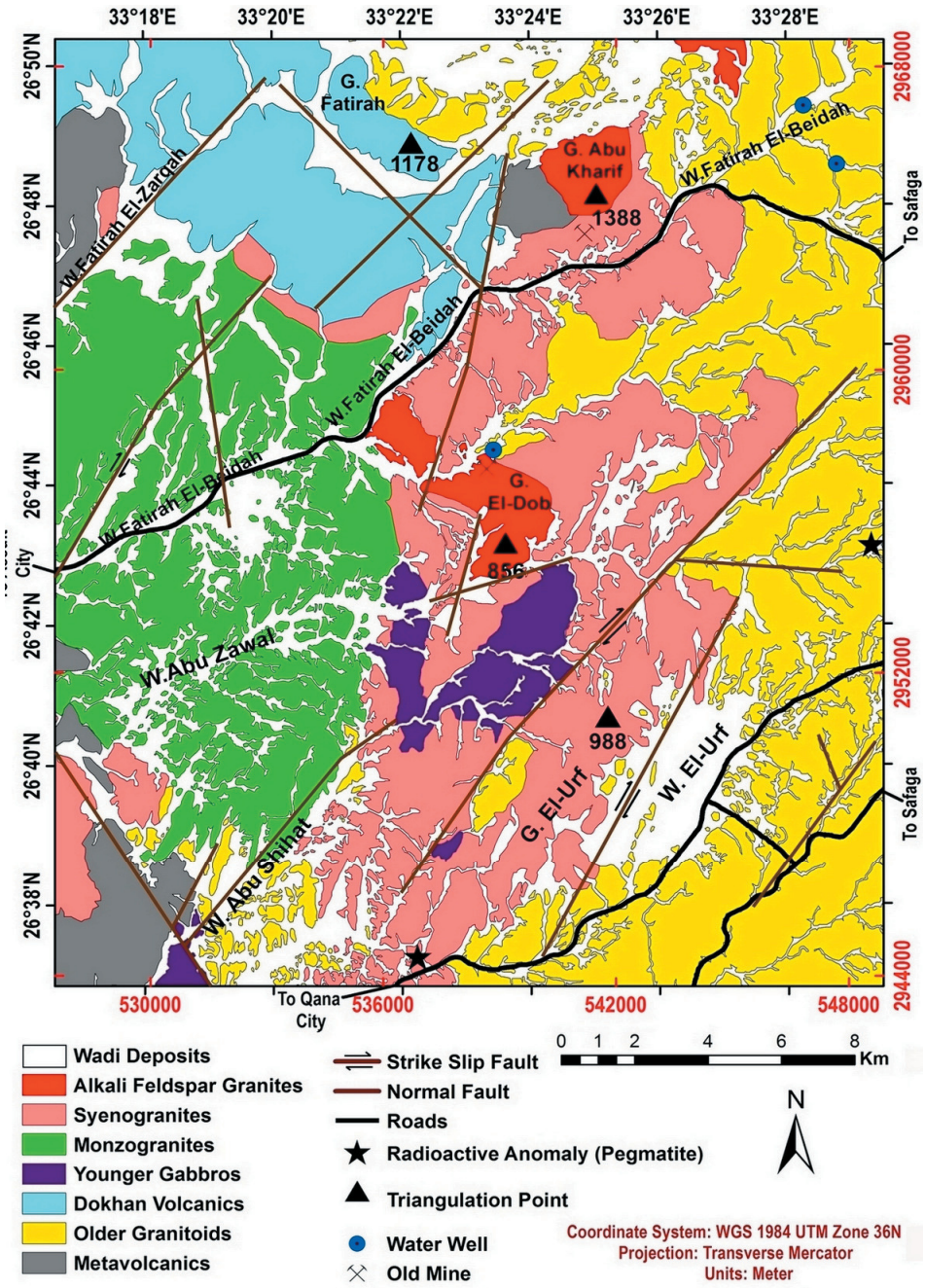

Fig. 37: Detailed geological map of W. Fatirah area based on remote sensing followed by field, petrographic and radiometric work verification

concerned in younger gabbros, metavolcanics, Dokhan volcanics and monzogranites. B) Phyllic alteration zones are mainly associated with older granitoids and parts of syenogranites at the north of G. El Dob, and C) Gossan is mainly concerned in younger granites (syenogranites and Alkali feldspar granites) and older granitoids. Four hydrothermal alteration minerals (chlorite, kaolinite, illite, and hematite) were successfully delineating using Feature-Oriented Principle Components Selection (FPCS). The Principal Component Analysis (PCA) highlighting the subtle spectral differences between different rock units within the study area especially the metavolcanics and younger gabbros.

The radioelements maps obtained from the airborne gamma-ray spectrometric data, participate in the lithological mapping of the exposed rock units more or less in harmony with the ASTER and Landsat-8 data results. Based on the fieldwork verifications, petrographic investigations, remote sensing processed data products of Landsat-8 and ASTER, spatial distribution and contact relationships, the main rock units of the study area are represented by metavolcanics, older granitoids, Dokhan volcanics, younger gabbros, younger granites (monzogranites, syenogranites, and alkali-feldspar granites) and post granitic dikes and pegmatites. The radioactive anomalies are mainly related to the younger granites and pegmatite bodies that associated with ferrugination (iron oxides and hydroxides alteration). The most promising radioactivity are delineated as pegmatite bodies at W. Abu Zawal and W. Abu Shihat.

REFERENCES

Abdeen, M.M. and Greiling, R.O., 2005. A Quantitative structural study of late pan-African compressional deformation in the Central Eastern Desert (Egypt) during Gondwana assembly. Gondwana Research, 8, 457-471.

Abdeen, M.M.; Thurmond, A.K.; Abdelsalam, M. and Stern, B., 2001. Application of ASTER band-ratio images for geological mapping in arid regions; The Neoproterozoic Allaqi Suture, Egypt. Geol. Soc. Am., 33, 1-289.

Abdel Ghani, I.M., 2020. The application of Landsat-8 imagery and airborne Gamma-ray spectrometric data for lithological mapping of Gabal Nuqara area, Central Eastern Desert, Egypt. J. North for Basic and Applied Sciences (JNBAS), Northern Border Univ., KSA, (In Press).

Abdelsalam, M.G.; Stern, R.J. and Berhane, W.G., 2000. Mapping gossans in arid regions with Landsat TM and SIR-C images: the Beddaho Alteration Zone in northern Eritrea. J. Afr. Earth Sci., 30, 903-916.

Abrams, M.J.; Brown, D.; Lepley, L. and Sadowski, R., 1983. Remote sensing of porphyry copper deposits in Southern Arizona. Econ. Geol., 78, 591-604.

Abu Zeid, H.T., 1991. The late Precambrian Dokhan volcanics of Egypt: Subducted-related or rift-related. 4th Ann. Meet. Miner. Soc. Egypt, Cairo, Abst.

Acharya, T. and Mallik, S.B., 2012. Analysis of lineament swarms in a Precambrian metamorphic rocks in India. J Earth Syst. Sci., 121(2), 453-462.

Aero-Service, 1984. Final operational report of airborne magnetic/ radiation survey in the Eastern Desert, Egypt, for the Egyptian General Petroleum Cooperation. Aero Service, Houston, Texas, April, 1984, six volumes.

Akaad, M.K. and El-Ramly, M.F., 1961. Geological history and classification of the basement rocks of Central Eastern Desert of Egypt. Ann. Geol. Surv. Egypt, 9, 24p.

Arnous, M. and Sultan, Y., 2014. Geospatial technology and structural analysis for geological mapping and tectonic evolution of Feiran-Solaf metamorphic complex, South Sinai, Egypt. Arab J. Geosci., 7, 3023-3049.

Badr, Y.S, 2017. Application of remote sensing technique in geologic mapping of hydrothermal alteration zones and possible radioactive poten-

tialities at Ras Barud - Um Tagher area, North Eastern Desert, Egypt. Ph.D. Thesis, Fac. Sci., Menoufiya Univ., Egypt, 164p.

Boyle, R.W., 1982. Geochemical prospecting for thorium and uranium deposits. Geological Survey Canada. Elsevier Scientific Publishing Company.

Crosta, A.P. and Moore, J.M., 1989. Enhancement of Landsat Thematic Mapper imagery for residual soil mapping in SW Minas Gerais State Brazil: A prospecting case history in greenstone belt terrain. Proceedings of the 7th Thematic Conference on Remote Sensing for Exploration Geology, Calgary, 1173-1187.

Daviz, J.D. and Guilbert, J.M., 1973. Distribution of radioelements potassium, uranium and thorium in selected porphyry copper deposits. Economic Geology, 68, 145-160.

Dawoud, M.; Abdel Ghani, I.M.; Elsaid, M. and Badr, Y.S., 2017. The integration of ASTER imagery and airborne gamma-ray spectrometry in lithological discrimination of Ras Barud - Um Tagher area, north Eastern Desert, Egypt. International Journal of Innovative Science, Engineering & Technology, 4 (9), 9-23.

Dixon, T.H., 1979. The evolution of continental crust in the late Precambrian Egyptian Shield. Ph.D. Thesis, Univ. Calif., San Diego, 230p.

Duval, J.S., 1983: Composite colour images of aerial gamma-ray spectrometric data. Geophysics, 48, 722-735.

Elawadi, I.A.; Ammar, A.A. and Elsirafy, A., 2004. Mapping surface geology using airborne gamma-ray spectrometric survey data: A case study. Proc. 7th SEGI International Symposium-Imaging Technology, Sendai, Japan, 349-354.

El-Gaby, S.; List, F.K. and Tehrani, R., 1988. Geology evolution and metallogenesis of the Pan African belt in Egypt. In: El-Gaby, S. and Greiling, R.O., (eds.). The Pan African belt of northeast Africa and adjacent areas. Viewing, Berlin, 17-70.

El-Rakaiby, M. 1993. Igneous rock-type discrimination from ratioed Landsat Thematic Mapper images of Southern Sinai, Egypt. The Egyptian Journal of Remote Sensing and Space Sciences, 1, 41-54.

El-Said, M., 2014. The application of Thermal Remote Sensing Imagery for studying uranium mineralization: A new exploratory approach for developing the radioactive potentiality at El-Missikat and El-Eridiya district, Central Eastern Desert, Egypt. Ph.D. Thesis, Fac. Sci., Damietta Univ., Egypt, 229 p.

El-Sharkawy, M.A.; Abu Zeid, H.T.; El-Bayoumi, R.M.; Shaalan, M. and Khalaf, E.A., 1991. On the volcanic rocks of Gabal Dokhan, Eastern Desert, Egypt. 4th Ann. Meet. Mineral. Soc. Egypt, Cairo, Abst., p.6.

El-Shazly, E.M., 1964. On the classification of the Precambrian and other rocks of magmatic affiliation in Egypt. XXII Inter. Geol. Congr. Proc. Sect., India, 10, 88-101.

Fullagar, P. and Greenberg, J., 1978. Egyptian younger granites: A single period of plutonism. Prec. Res., 6(1), A22.

Galvao, L.S.; Filho, R.A. and Vitorello, I., 2005. Spectral discrimination of hydrothermally altered materials using ASTER short-wave infrared bands: Evaluation in a tropical savannah environment. International Journal of Applied Earth Observation and Geoinformation., 7, 107-114.

Gass, I.G., 1981. Pan-African (Upper Proterozoic) Plate tectonics of the Arabian shield. In: Kroner, A. (ed.) Precambrian Plate-Tectonic, Elsevier, Amesterdam, 378-405.

Gossens, M.A., 1992. Petrogenesis of the mineralized granitic intrusion near Los Santos, Western Spain, and remote sensing and data integration as a tool in regional exploration for granite related mineralization. Geologica Ultraiectina, 89, 1-148.

Hashad, A.H., 1980. Present studies of geochronological data on the Egyptian basement complex. Inst. App. Geol. Bull., Jeddah, 4, 31-46.

Hume, W.F., 1935. Geology of Egypt, Part II. The later plutonic and intrusive rocks. Geol. Surv. Egypt., 301- 688.

Hussein, A.A.; Ali, M.M. and El-Ramly, M.F., 1982. A proposed new classification of the granites of Egypt. J. Volcanol. Geotherm. Res., 14, 187-198.

Jensen, J.R., 1986. Introductory Digital Image Processing: A Remote Sensing Perspective, Prentice-Hall, Englewood Cliffs, NJ.

Kuhns, R.J., 1986. Alteration styles and trace element dispersion associated with the Golden Giant deposit, Ontario, Canada. Geology of Gold, 86, 340-354.

Loughlin, W.P., 1991. Principal Component Analysis for alteration mapping. Photogrammetric Engineering and Remote Sensing, 57, 1163-1169.

Rogers, J.J.W. and Greenberg, J.K., 1983. Summary of recent work on Egyptian younger granites. Ann. Geol. Surv. Egypt, 13, 185-191.

Rowan, L.C.; Hook, S.J.; Abrams, M.J. and Mars, J.C., 2003. Mapping hydrothermally altered rocks at Cuprite, Nevada using advanced spaceborne thermal emission and reflection radiometer (ASTER), a new satellite-imaging system. Econ. Geol., 98 (5), 1019-1027.

Rowan, L.C.; Mars, J.C. and Simpson, C.J., 2005. Lithologic mapping of the Mordor NT, Australia ultramafic complex by using the Advanced Spaceborne Thermal Emission and Reflection Radiometer (ASTER). Remote Sens. Environ., 99 (1-2), 105-126.

Sabins, F.F., 1987. Remote Sensing Principles and Interpretation, 2nd edition. Freeman New York.

Schetselaar, E., 2001. On preserving spectral balance in image fusion and its advantages for geological image interpretation. Photogrammetric Engineering and Remote Sensing, 67 (8), 925-934.

Schroeter, T.G., 1995. Porphyry Deposits of The Northwestern Cordillera of North America. Geol. Soc. CIM, 888p.

Stern, R.J., 1979. Late Precambrian crustal environments as reconstructed from relic igneous minerals, Central Eastern Desert of Egypt. Ann. Geol. Surv. Egypt, 9, 9-31.

Sweha, R.N.A., 2014. Integrated geophysical and remote sensing studies to detect mineralization zones at Gabal Dara area, Eastern Desert, Egypt. M.Sc. Thesis, Fac. Sci., Zagazig Univ., Egypt, 154p.

Takla, M.A.; Basta, E.Z. and Fawzi, E., 1981. Characterization of the older and younger gabbros of Egypt. Delta J. Sci., Tanta Univ., 5, 279-314.

Velosky, J.C.; Stern, R.J. and Johnson, P.R., 2003. Geological control of massive sulfide mineralization in the Neoproterozoic Wadi Bidah shear zone, Southwestern Saudi Arabia from orbital remote sensing and field studies. Precambrian Res., 123, 235-247.

Welman, P., 1998. Mapping of granite batholith using geological and remotely sensed data: The Mount Edgar Batholith, Pilbara Craton. Exploration Geophysics, 9, 643-648.

Wilford, J.R., 1992. Regolith mapping using integrated Landsat TM imagery and high resolution gamma-ray spectrometric imagery - Cape York Peninsula. Bureau of Mineral Resources, Record 1992/78.

Xu, Y.; Lin, Q.; Shao, Y. and Wang, L., 2004. Extraction mechanism of alteration zones using ASTER imagery. IGARSS 2004. 2004 IEEE International Geoscience and Remote Sensing Symposium, Anchorage, AK 2004, 6, 4174-4175.

تطبيقات الإستشعار عن بعد فى التخريط الجيولوجى والاشعاعي لصخور ماقبل الكامبري بمنطقة وادى فطيره، شمال الصحراء الشرقية، مصر

محمد صالح حمد، نهلة احمد الشلالي، اسماعيل محمدعبدالغني، ياسر صلاح بدر و صابرين عمرو سيد

تجمع الدراسة الحالية بين التحليل الطيفي لبيانات الاقمار الصناعية (لاندسات-٨ والاستر) وطيف أشعة جاما المحمولة جواً متبوعاً بالعمل الحقلي التفصيلى وكذلك الدراسات الميكروسكوبية بغية التخريط الجيولوجي لمنطقة وادي فطيره، شمال الصحراء الشرقية، مصر.

خضعت المرئيات الفضائية المستخدمة للعديد من التطبيقات (المركبات اللونية الكاذبة، تحليل المكون الرئيسي للطيف، تقنية كروستا وكذا النسبة بين حزم الاطياف المتعددة) والتي أسفرت جميعها عن إظهار الإختلافات الدقيقة بين جميع الوحدات الصخرية مما ساعد بشكل كبير في عملية التخريط الجيولوجي لمنطقة الدراسة.

اظهرت بيانات أشعة جاما المحمولة جواً في هيئة خرائط كنتورية توزيع اليورانيوم والثوريوم وكذا البوتاسيوم في الوحدات الصخرية المنكشفة بالمنطقة ومعالجتها إحصائياً ساهم في عملية التمييز بين صخور المنطقة وخصوصاً الجرانيتات الحديثة.

تم التحقق من جميع النتائج خلال العمل الحقلي المكثف وجمع العينات التي خضعت للدراسات المعملية (ميكروسكوبية واشعاعية) مفصلة مع التركيز على الجرانيتات نظراً لاحتوائها على أعلى قراءات اشعاعية بمنطقة الدراسة.

أعتماداً على جميع ما سبق ذكره، تم عمل خريطة جيولوجية تفصيلية بمقياس رسم (١:٥٠٠٠٠) تبين الوحدات الصخرية علي النحو التالي: البركانيات المتحولة (الأقدم)، الجرانيتيدات القديمة، بركانيات الدخان، الجابرو الحديث، الجرانيتات الحديثة ويقطع هذه الوحدات اجسام من البيجماتيت وعدة قواطع (الأحدث).

تم عمل عدد من الخرائط تبين بعضاً من معادن التغيرات الحارمائية إضافة إلى تحديد عدد من الشاذات المشعة في وادي أبوزوال ووادي أبو شيحات.